# Precipitation Behavior of Super Duplex Stainless Steel in Friction-Stir-Welding Processes

Sugimoto, Itto
Department of Applied Science for Electronics and Materials. Hitachi Ltd.

Saito, Hiakaru
Department of Advances Materials Science, Kyushu University : Assistant Professor

Hata, Satoshi
Department of Advances Materials Science, Kyushu University : Professor

https://doi.org/10.15017/2544129

出版情報：九州大学大学院総合理工学報告. 40 (1), pp.7-14, 2018-09. Interdisciplinary Graduate School of Engineering Sciences, Kyushu University
バージョン：
権利関係：

九州大学大学院総合理工学府報告
第40巻 第1号 7-14 頁 平成30年9月

Engineering Sciences Reports, Kyushu University
Vol. 40, No. 1, pp. 7-14, SEP, 2018

# Precipitation Behavior of Super Duplex Stainless Steel in Friction-Stir-Welding Processes

Itto SUGIMOTO*1, † Hikaru SAITO*2 and Satoshi HATA*2
†E-mail of corresponding author: itto.sugimoto.nu@hitachi.com

(Received July 19, 2018, accepted July 20, 2018)

To investigate the precipitation behavior of super duplex stainless steel in its weld by friction stir welding (FSW) at a low welding speed, we carried out microstructural observation and analysis. An intermetallic compound phase, σ, was observed in the heat affected zone (HAZ). The σ phase precipitated at the interfaces between δ-Fe (ferrite) and γ-Fe (austenite) grains 1 - 2 mm away from the stir zone (SZ) / HAZ boundary. On the other hand, the $Cr_2N$ phase was observed together with the belt-like γ-Fe grain aggregates in the vicinity of the advancing side (AS) of the SZ. The other intermetallic phase, χ, was also observed at a triple point of γ-Fe grains. One can interpret that the precipitation of the $Cr_2N$ and χ phases correlates with the transformation of δ-Fe to γ'-Fe (secondary austenite).

**Key words:** *Super duplex stainless steel, Friction stir welding (FSW), Sigma (σ) phase, Chi (χ) phase, Chromium nitride, Electron back-scatter diffraction (EBSD), Transmission electron microscopy (TEM)*

## 1. Introduction

Super duplex stainless steels are the next generation high durability structural material having both high strength and high corrosion resistance, and are expected to use for plants, water treatment equipment, pipelines, etc. The microstructure of duplex stainless steels consists of ferrite (δ-Fe) and austenite (γ-Fe), and their volume ratio is approximately 1: 1. The duplex stainless steels are mainly Fe-Ni-Cr ternary systems containing other elements to improve strength, corrosion resistance, workability and weldability. For example, pitting corrosion resistance of stainless steel is enhanced by adding a significant amount of Cr, Mo, W and nitrogen. The pitting resistance equivalent number (PREN) expressed by the following formula is an index showing the pitting corrosion resistance of stainless steel. Super duplex stainless steels are those of duplex stainless steels with PREN of 40 or more [1]:

$$\mathrm{PREN} = 1\%\mathrm{Cr} + 3.3(\%\mathrm{Mo} + 0.5\%\mathrm{W}) + 16\%\mathrm{N}.$$

Although super duplex stainless steels have excellent material properties, their corrosion resistance is remarkably impaired by precipitation of an intermetallic phase, σ, in welding processes [1], [2]. Fig. 1 shows that optical microscopic images of super duplex stainless steel used in this study. In Fig. 1 (a), a base material without heat treatment shows a two-phase structure, ferrite (δ-Fe) and austenite (δ-Fe), with a lamellar morphology. On the other hand, Fig. 1 (b) shows a test piece after heating at 800 °C for 30 min. The σ phase forms in the lamellar structure, as recognized in the darkest region. One can interpret that the σ phase precipitated during the heat treatment. The interfacial energy of the duplex stainless steel is highest at the interface between δ-Fe and γ-Fe, and the σ phase precipitates preferentially at the δ / γ interfaces [3], [4]. The precipitation of the σ phase is related to the formation of the secondary austenite, γ'-Fe [5], [6]. That is, Ni is partitioned to the γ'-Fe grains during the transformation from δ-Fe to γ'-Fe due to the differences in solubility of each element. On the other hand, Cr and Mo are discharged from γ'-Fe and the σ phase containing a significant amount of Cr

---

*1 Department of Applied Science for Electronics and Materials. Hitachi Ltd.
*2 Department of Advances Materials Science

and Mo precipitated. Fig. 1 (b) also shows that the σ phase precipitates to erode δ grains.

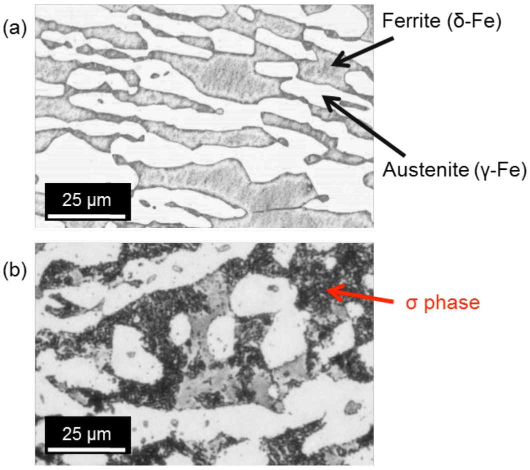

**Fig. 1** Cross-sectional optical microscopy images of a super duplex stainless steel. (a) A base material without heating and (b) a heat-treated material (800°C for 30 min).

The present study focuses on friction stir welding (FSW) of super duplex stainless steel. The FSW is a metal bonding method invented in the Welding Institute (TWI) in 1991, and its process is a kind of solid phase bonding not through the process of melt solidification[7]. Joining by the FSW was initially applied to low melting point metals such as aluminum alloys. Its joining part has little welding trouble such as grain coarsening, residual stress, deformation, porosity and solidification crack after construction. Therefore, the FSW of high melting point materials such as various steels and titanium alloys has been vigorously studied. Fig. 2 shows (a) a bird's-eye view of the FSW joining and (b) a schematic cross-sectional image of the weld. The FSW device consists of rotation tools with a probe and a shoulder at the tip. The rotation tool is inserted into the weld material and is moved along a joining line under a loaded state. The softened parts by frictional heat are stirred and plastically flowed, and then joined by recombining at the back of the rotation tool.

The cross-sectional structure after the FSW consists of a stir zone (SZ), a heat affected zone (HAZ) and a base material. The HAZ formed by the FSW can be divided into a thermo-mechanically affected zone (TMAZ), which is affected, by plastic deformation and a HAZ with no influence of the plastic flow. One should notice that the left and right sides of the cross-sectional image of the welds do not show a symmetrical structure in many cases. The left and right sides are distinguished as the followings respectively: an advancing side (AS) where the directions of the tool rotation and the material joining coincide with each other and a retreating side (RS) where these two directions are opposite to each other.

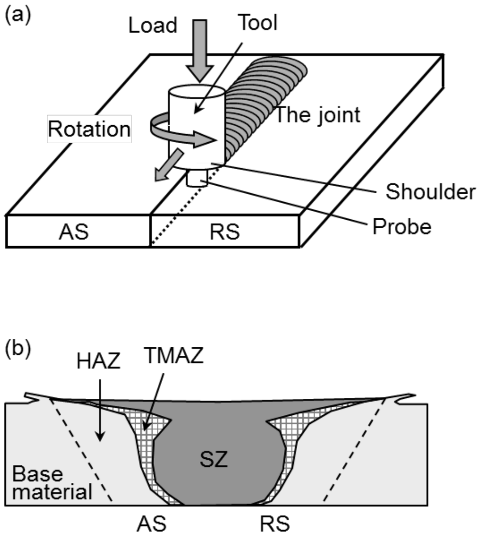

**Fig. 2** (a) A bird's eye view of joining by the FSW and (b) a schematic cross-section of the weld formed by the FSW.

The FSW of super duplex stainless steels is challenging to join them, but there have been several reports after developments of various high durability tools. According to these reports [8)~11)], the welds of super duplex stainless steel consist of fine grains of δ-Fe and γ-Fe. However, as far as the authors' knowledge, there has been no report on precipitates in the FSW welds of super duplex stainless steels. In this study, the FSW is conducted on a super duplex stainless steel at a lower welding speed than usual, and its weld part was observed in detail by electron microscopy. Based on the electron microscopy experiment, we will clarify the precipitation behavior at the weld of the super duplex stainless steel, which is an indispensable knowledge for using the welded material safely.

## 2. Experimental procedure

The super duplex stainless steel prescribed in UNS-S32750 was used for the present study. A rolled material, which has a length of 300 mm, a width of 100 mm and a thickness of 12 mm, was prepared, and a bead-on-plate test of the FSW with a welding length of 200 mm was carried out at the center of the adjacent materials to join.

**Table 1** The chemical composition of the super duplex stainless steel (UNS-S32750) used in the present study.

(wt%)

| Fe | C | Si | Mn | P | S |
|---|---|---|---|---|---|
| Bal. | 0.017 | 0.50 | 0.84 | 0.024 | 0.001 |
| Cu | Ni | Cr | Mo | N | |
| 0.19 | 6.9 | 25.0 | 4.0 | 0.24 | |

Table 1 shows the chemical composition of the super duplex stainless steel used in the present study. The nitrogen concentration, 0.24 wt% N, is higher than those of other stainless steels and is adjusted so that the PREN described as formula (1) becomes 42.5 or more.

In the welding test of the FSW, the rotation speed was 400 rpm, the rotation tool tilt angle was 3°, and the plunging depth was 5.1 mm. Fig. 3 shows a rotation tool made of a commercially available ceramic material, SIALON (Si-Al-O-N), with a probe length of 4.5 mm and a shoulder diameter of 18.0 mm. The welding speed was 0.42 mm / s which is 1/4 of the proper speed of 1.7 mm / s. The welding speed is an important parameter to obtain good weld joints by the FSW. For the present experimental settings and materials, no welding defect was formed by setting the welding speed to 1.7 mm/s or less. Cross-sectional specimens of the weld from the central part of the weld bead were prepared for microstructural observations. Firstly, the sample was electrolytically etched with 10 kmol/m$^3$ KOH solution for macroscopic characterization using optical microscopy. Secondary, micrometer-scale microstructural characterizations have been carried out using scanning electron microscopy (SEM) combined with an electron back-scatter diffraction (EBSD) technique. Thirdly, nanometer-scale microstructural characterizations have been performed using transmission electron microscopy (TEM) and scanning transmission electron microscopy (STEM). A focused ion beam (FIB) sampling technique was utilized for the TEM/STEM specimen preparation.

Phase stability calculations were carried out using Thermo-calc. software to evaluate possible precipitates formed during the FSW process. Kinetic behaviors of the precipitates were also calculated using JmatPro software. For both the calculations, the same chemical composition as the material used in the experiment (Table 1) was assumed.

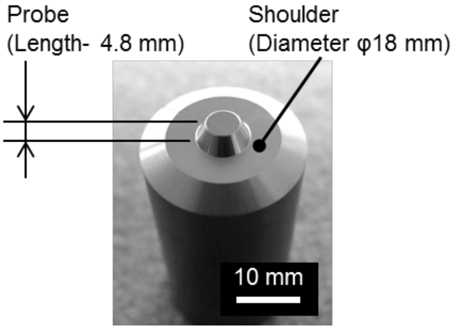

**Fig. 3** A rotation tool for the FSW made of SIALON.

## 3. Results and discussion

### 3.1 Calculated phase stability and precipitation kinetics

Fig. 4 shows calculated mole fractions of the thermal equilibrium phases as a function of temperature and Fig. 5 shows calculated time-temperature-transformation (TTT) diagrams for the possible precipitates in the present alloy system. The plots in Fig. 5 express the conditions under which the volume fractions of the phases are more than 0.5%. Let us explain the phases shown in these figures. δ-Fe and γ-Fe are the matrix phases of the duplex steel. σ is the tetragonal intermetallic phase described as Fe-Cr(-Mo).

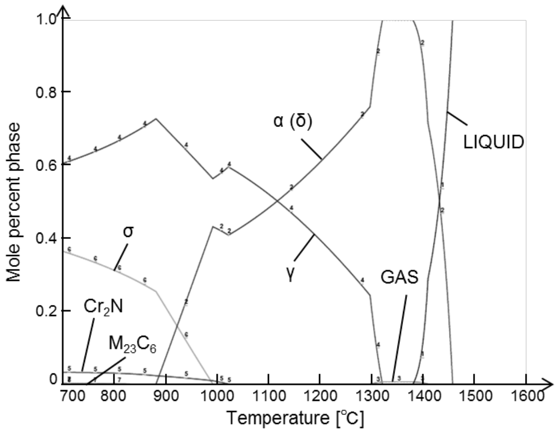

**Fig. 4** Calculated mole fractions of the thermal equilibrium phases of the super duplex stainless steel as a function of temperature.

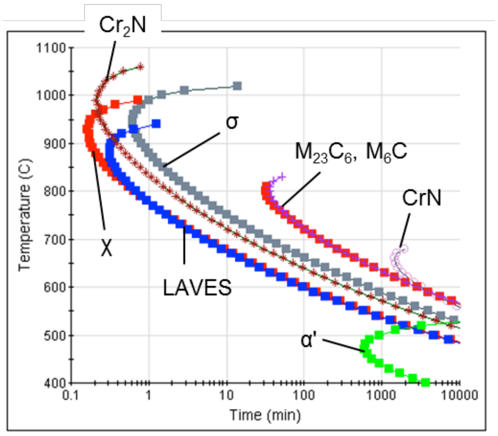

**Fig. 5** Calculated time-temperature-transformation (TTT) diagrams for the possible phases in the super duplex stainless steel.

χ is a cubic intermetallic phase having a composition of $Fe_{36}Cr_{12}Mo_{10}$. Because the χ phase is a metastable phase, it does not appear in Fig. 4. $Cr_2N$ is a hexagonal nitride phase commonly observed in super duplex stainless steels containing significant amounts of nitrogen. CrN is a cubic nitride phase. The LAVES phase is a cubic or hexagonal intermetallic phase described as $AB_2$.

As for Fig. 4, the mole ratio between δ-Fe and γ-Fe changes at higher than 1000 °C while no precipitation is expected in this high-temperature range. On the other hand, the intermetallic σ phase and the nitride $Cr_2N$ phase are also main thermal equilibrium phases at 1000 °C or lower. The volume fraction of the σ phase increases up to 0.4 at 700 °C.

As for Fig. 5, the σ, $Cr_2N$, χ and LAVES phases precipitate after relatively short durations than $M_{23}C_6$, $M_6C$ and CrN phases in a temperature range of 700-1000 °C. The $Cr_2N$ phase precipitates in much shorter durations than those for the CrN phase.

### 3.2 Microstructural observations

Fig. 6 shows cross-sectional views of the weld. By setting the low welding speed, 0.42 mm/s, no welding defect occurred. However, Fig. 6(a) shows unknown image contrast in the SZ near the AS. This unknown image contrast showing the belt-like morphology is recognized in both the optical microscopy (a) and SEM (b) images and notably different from the uniform image contrast of the (δ-Fe + γ-Fe) two-phase matrix. In the following EBSD analysis, area A and area B denoted in Fig. 6 (b) were selected for the fields of view. Area A is located 2.0 mm away from the SZ/TMAZ interface in the HAZ outside the AS, and area B is in the belt-like structure of the SZ.

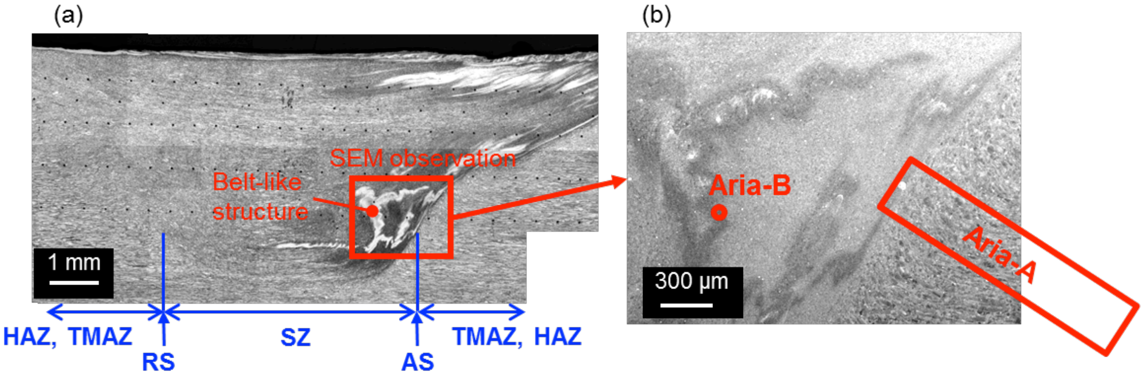

**Fig. 6** Cross-sectional optical microscopy (a) and SEM (b) images of the FSW sample under the welding speed of 0.42 mm/s.

Fig. 7 demonstrates the SEM-EBSD analysis in area A including the TMAZ/HAZ. No precipitate was recognized near the SZ/TMAZ interface. However, some phases other than the δ-Fe and γ-Fe matrix phases were observed in the HAZ being 1.5 mm away from the SZ/TMAZ interface. The observed precipitates showed brighter contrast than the matrix grains in the SEM images and confirmed to be of the σ phase, as displayed in yellow on the EBSD phase map. The σ phase precipitates from the δ-Fe (red) / γ-Fe (green) interface. This fact coincides with the precipitation behavior of σ phase during heat treatments reported previously [3), 4)]. The precipitation of the σ phase in the HAZ was also recognized at a location about 1 mm away from the SZ/TMAZ interface at the RS. The calculated results in Fig. 5 and Fig. 6 indicated that the σ phase is most likely to precipitate around 950 °C and the alloy should be kept at the temperature for more than 1 min to promote the σ precipitation. In the weld, the region 1-2 mm away from SZ was kept just in that temperature region, and the σ phase precipitated.

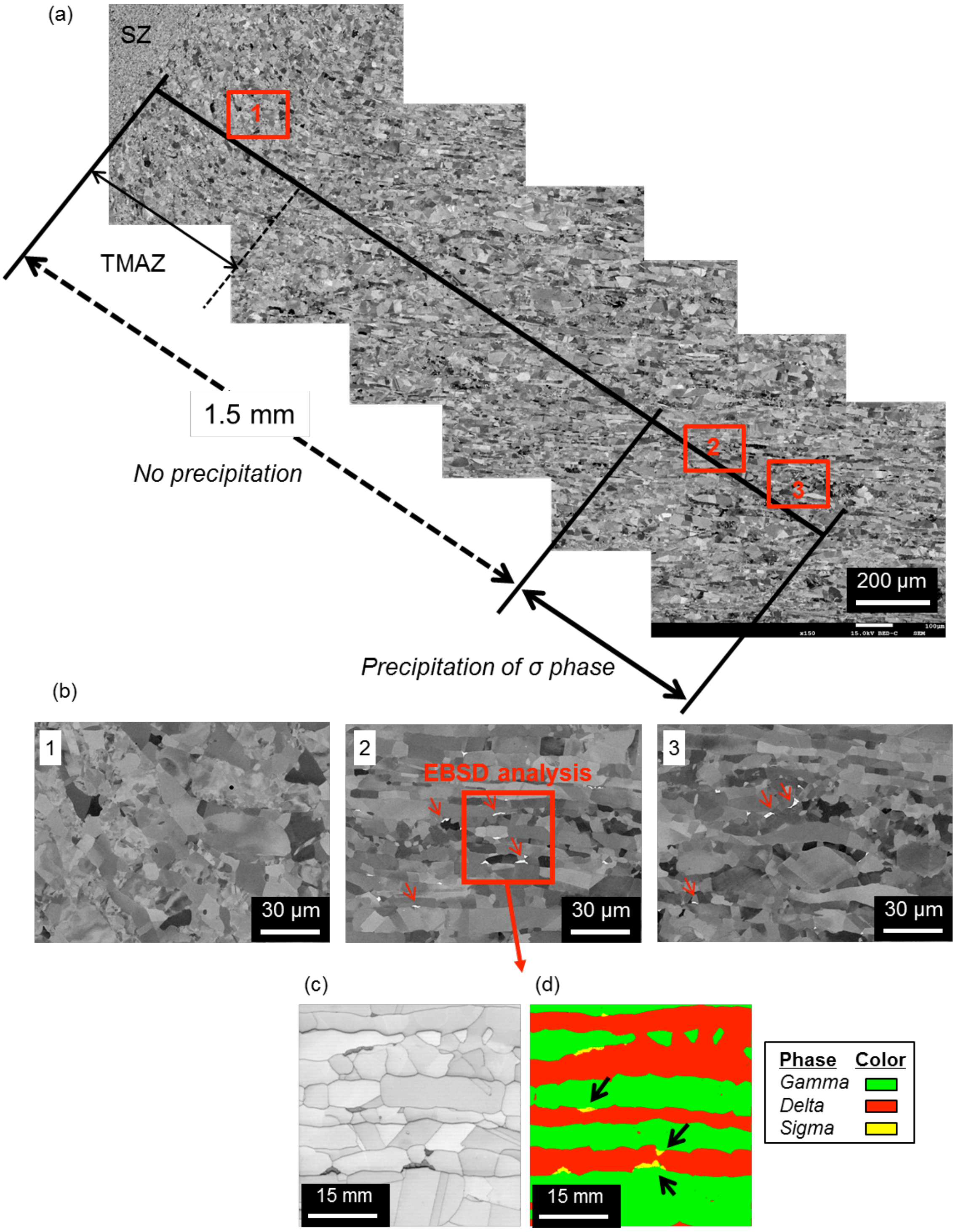

**Fig. 7** SEM-EBSD analysis of area A denoted in Fig. 6(b) including the TMAZ/HAZ. (a) Low-magnification SEM images, (b) magnified views of areas 1, 2 and 3 depicted with rectangles in (a), (c) an image quality map and (d) a phase map acquired from a square area denoted in area 2 of (b).

Fig. 8 demonstrates the SEM-EBSD analysis in area B of the SZ. The SZ shows a microstructure in which the crystalline grains are small: a few micrometers as a whole. The belt-shaped structure showing the darker contrast than the matrix is notably coarser than the grain sizes at the SZ. This coarse belt-shaped structure is interpreted as a trace of the stirred fluid. The EBSD analysis found that the belt-shaped structure is an aggregate of γ-Fe in which δ-Fe does not exist even though the surrounding matrix consists of the (γ-Fe + δ-Fe) two-phase structure. Furthermore, fine $Cr_2N$ precipitates indicated by the blue color in Fig. 8 (c) are formed in the grain boundaries of γ-Fe. It should be noted that there is a microstructure composed of $Cr_2N$ and γ-Fe phases which has a higher solid solubility of nitrogen than that of δ-Fe.

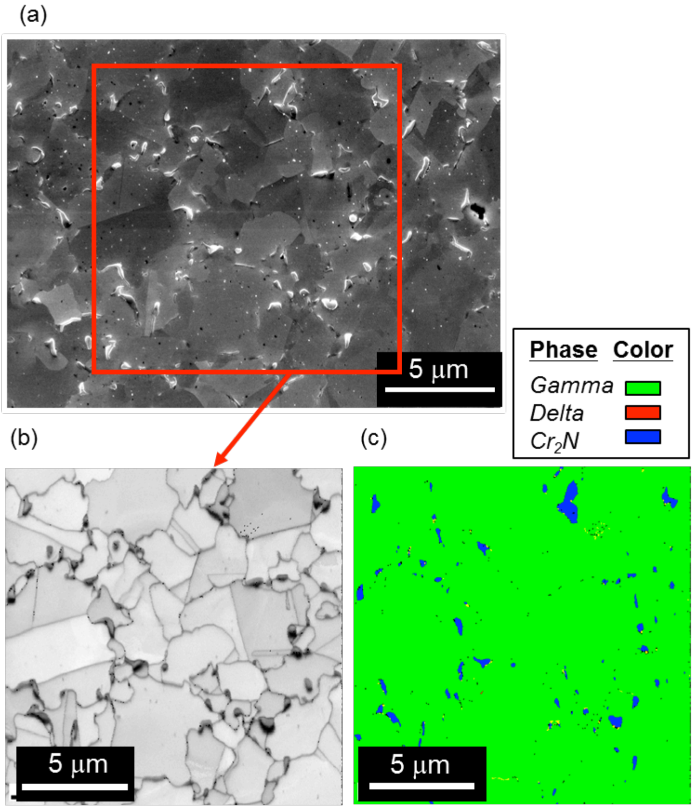

Image Quality map

Phase map

**Fig. 8** SEM-EBSD analysis of area B denoted in Fig. 6(b) in the belt-shaped structure near the SZ/TMAZ interface at the AS. (a) An SEM image, (b) an image quality map and (c) a phase map acquired from a square region depicted in (a).

Fig. 9 demonstrates STEM/TEM analysis of an area showing the fine $Cr_2N$ precipitates at which the specimen was prepared by FIB. The STEM high-angle annular dark-field (HAADF) image in Fig. 9(a) indicates that $Cr_2N$ showing the darker image intensity precipitates at the grain boundaries of the γ-Fe matrix. Fig. 9(b) shows a magnified view of the square area depicted in Fig. 9(a). At the triple junction of the γ-Fe grains, a precipitate showing the brighter image intensity is formed with the two adjacent $Cr_2N$ particles. Fig. 9(c) shows a TEM bright-field (BF) image of the same field of view as in Fig. 9(b). A selected area diffraction pattern in Fig. 9(e) acquired from the precipitate at the triple junction denoted as area 2 in Fig. 9(c) is different from a diffraction pattern in Fig. 9(d) acquired from area 1 in the γ-Fe matrix. Indexing the diffraction pattern in Fig. 9(e) revealed that the precipitate at the triple junction is of the χ phase. The STEM/TEM analysis in Fig. 9 indicates the existence of aggregates of the γ-Fe matrix containing the grain boundary precipitates of $Cr_2N$ and χ phases in the SZ. It is interpreted that the $Cr_2N$ phase in the form of sheets precipitated at grain boundaries of the γ-Fe matrix and the χ phase precipitated at triple junctions of the γ-Fe matrix.

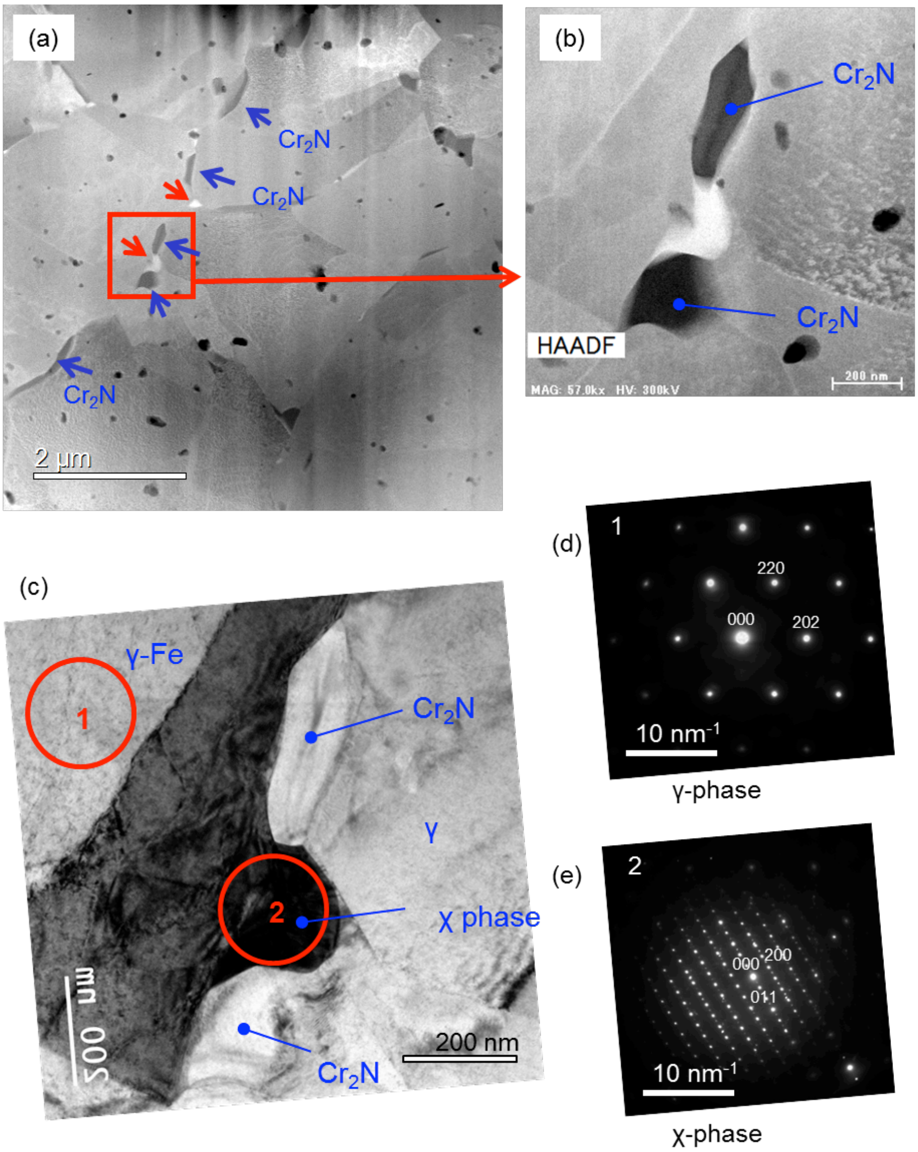

**Fig. 9** STEM/TEM analysis of an area showing $Cr_2N$ precipitates. (a) A STEM-HAADF image, (b) a magnified view of a square area depicted in (a), (c) a TEM-BF image, and (d) and (e) selected area diffraction patterns acquired from areas 1 and 2 depicted respectively in (c).

The precipitation of $Cr_2N$ is commonly observed in super duplex stainless steels containing a large amount of nitrogen. Ramirez et al. [12)] investigated the precipitation behavior of $Cr_2N$ and reported the following relationship between $Cr_2N$ and γ'-Fe (secondary austenite) phases: $Cr_2N$ nucleates from δ-Fe phase side at δ-Fe / γ-Fe interfaces. Because the $Cr_2N$ precipitation consumes nitrogen in the γ-Fe matrix, the grain boundaries of γ-Fe containing the $Cr_2N$ precipitates reduce nitrogen concentrations. As the nitrogen contained in the γ-Fe matrix diffuses toward the δ-Fe / γ-Fe interfaces, the δ-Fe matrix partially transforms to austenite which is called secondary austenite, γ'-Fe. The phase transition processes described above is summarized as follows:

$$\delta + \gamma \rightarrow (\delta + Cr_2N) + \gamma \rightarrow (\delta + Cr_2N + \gamma') + \gamma.$$

In the present super duplex stainless steel,

$Cr_2N$ was observed in the aggregates of the austenite not containing δ-Fe phase. If the phase evolution proceeds along the reactions described above, the interpretation is possible: $Cr_2N$ nucleated at the grain boundary of the δ phase. At the SZ, the grain sizes of the (δ-Fe + γ-Fe) matrix became smaller to micrometer sizes during the friction stirring process. The δ-Fe phase around the $Cr_2N$ phase transformed to γ'-Fe because nitrogen diffusion from the γ-Fe phase stabilizes γ'-Fe than δ-Fe. As a result, aggregates consisting of the γ-Fe and γ'-Fe grains were formed around the $Cr_2N$ precipitates. Mo was also released when the δ-Fe phase transformed to γ'-Fe and the χ phase was then formed at the triple junctions of the γ'-Fe and δ-Fe grains by bounding Mo with the surrounding Fe and Cr.

Fig. 10 illustrates model precipitation sites revealed in this study. The σ phase precipitated in the HAZ about 1-2 mm away from the SZ which was not influenced by plastic flow during the FSW process. The $Cr_2N$ and the χ phase precipitated in the vicinity of the AS in the SZ, and aggregates of γ-Fe and γ'-Fe formed with the $Cr_2N$ and χ precipitates.

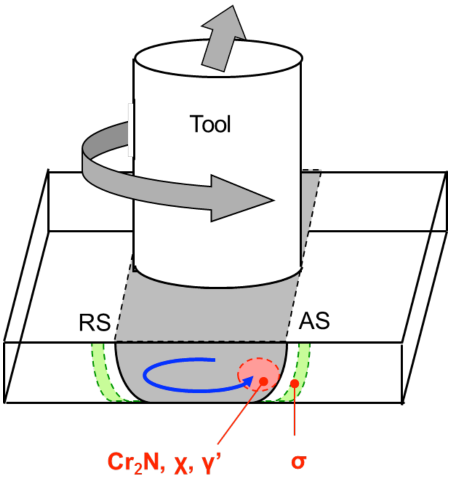

**Fig. 10** Model precipitation sites in the FSW weld.

The vicinity of the AS is a place where the plastic fluid circulating with the rotating tool accumulates, as shown in Fig. 10. It seems that the belt-like fluid as shown in Fig. 6 circled with the tool multiple times, was exposed in a heating environment for a long duration, and precipitated $Cr_2N$ grains. The calculated TTT diagram of Fig. 5 indicates that $Cr_2N$ precipitates at a high temperature in a short duration compared with the σ phase. Based on the calculation, $Cr_2N$ preferentially precipitated in the SZ, and the γ'-Fe phase and the χ phase formed secondarily. According to Escriba et al. 13), it is possible that the χ phase formed as a precursor stage of the σ phase. Since these precipitates influence material properties, it is necessary to optimize the FSW conditions for suppressing the precipitation as future work.

## 4. Conclusion

The precipitation behavior of super duplex stainless steel in the weld formed by the FSW at a low welding speed was investigated using optical and electron microscopy techniques. The results are shown below.

1) The σ phase precipitated in the HAZ which was 1-2 mm away from the interface with the SZ. The interface between the δ-Fe and γ-Fe phases is the precipitation site for the σ phase.
2) The $Cr_2N$ precipitated in the austenite aggregates with the belt-like morphology in the SZ near the AS. Also, the χ phase precipitated at a triple junction of the austenite grains.

## References

1) Gunn, R. N., *Duplex stainless steels (Microstructure, properties and applications), Abington Publishing*, p. 204, (1997).
2) Lopez, N., Cid, M. and Puiggali M., *Corrosion Science*, 41, pp. 1615–1631, (1999).
3) Lee, K. M., Cho, H. S. and Choi, D. C., *Journal of Alloys and Compounds*, 285, pp. 156–161, (1999).
4) Chen, T. H. and Yang, J. R., *Materials Science and Engineering A*, 311, pp. 28–41, (2001).
5) Angelini, E., Benedetti, B. D. and Rosalbino, F., *Corrosion Science*, 46, pp. 1351–1367, (2004).
6) Pohl, M., Storz, O. and Glogowski, T., *Materials Characterization*, 58, pp. 65–71, (2007).
7) Mishra, R. and Ma, Z., *Materials Science and Engineering R*, 50, pp. 1–78, (2005).
8) Sato, Y. S., Nelson, T. W., Sterling, C. J., Steel, R. J. and Petteresson, C.–O., *Materials Science and Engineering A*, 397, pp. 376–384, (2005).
9) Saeid, T., Abdollah-Zadeh, A., Assadi, H. and Malek-Ghaini, F. *Materials Science and Engineering A*, 496, pp. 262–268, (2008).
10) Saeid, T., Abdollah-Zadeh, A., Shibayanagi, T., Ikeuchi, K. and Assadi, H., *Materials Science and Engineering A*, 527, pp. 6484–6488, (2010).
11) Esmail-Zadeh, M., Shamanian, M., Kermanpur, A. and Saeid, T., *Materials Science and Engineering A*, 561, pp. 486–491, (2013).
12) Ramirez, A. J., Lippold, J. C. and Brandi, S. D., *Metallurgical and Materials Transactions A*, 34A, pp. 1575–1597, (2008).
13) Escriba, D. M., Morris, E. M., Plaut, R. L. and Padilha, A. F., *Materials Characterization*, 60, pp. 1214–1219, (2009).